State Diagrams of PBTTT Derivatives Mixed with PC61BM and Their Relevance for Organic Electronics: Influence of Incongruently Melting Co-crystals and Homocoupling Defects

DOI: 10.1002/smll.202410993
Handle: http://hdl.handle.net/1942/45657

State Diagrams of PBTTT Derivatives Mixed with $PC_{61}BM$ and their Relevance for Organic Electronics: Influence of Incongruently Melting Co-crystals and Homocoupling Defects

Zhen Liu*†, Jochen Vanderspikken, Koen Vandewal, Wouter Maes*, Bart Goderis, Erik Nies, Niko Van den Brande and Bruno Van Mele*

Dr. Z. Liu, Prof. N. Van den Brande, Prof. B. Van Mele

Lab of Physical Chemistry and Polymer Science (FYSC), Research group Sustainable Materials Engineering (SUME), Vrije Universiteit Brussel (VUB), Pleinlaan 2, B-1050 Brussels, Belgium

E-mail: bruno.van.mele@vub.be

† Present address: Key Laboratory of Transient Optics and Photonics, Xi'an Institute of Optics and Precision Mechanics (XIOPM), Chinese Academy of Sciences (CAS), Information road 17, Xi'an, Shaanxi, 710119, China

E-mail: liuzhen@opt.ac.cn

Dr. J. Vanderspikken, Prof. K. Vandewal, Prof. W. Maes

Institute for Materials Research (imo-imomec), Hasselt University, Hasselt, 3500, Belgium

Imec, imo-imomec, Diepenbeek, 3590, Belgium

E-mail: wouter.maes@uhasselt.be

Prof. B. Goderis, Prof. E. Nies

Polymer Chemistry and Materials Division, KU Leuven, Leuven, 3001, Belgium

Keywords: homocoupling-free alternating conjugated polymers, intercalation, eutectic-peritectic, rapid heat-cool DSC, temperature-resolved synchrotron XRD

Abstract

Double binary state diagrams of the benchmark semi-crystalline conjugated polymer PBTTT and its alkoxy derivatives PBTTT-OR-R and PBTTT-$(OR)_2$, mixed with $PC_{61}BM$, are constructed using Rapid Heat-Cool Differential Scanning Calorimetry and T-resolved synchrotron X-Ray Diffraction. The polymerization method is adapted to ensure the absence of homocouplings and obtain reliable state diagrams, supported by Flory-Huggins calculations. Co-crystallization always occurs at a 45:55 w/w%

polymer:$PC_{61}BM$ mixing ratio. All co-crystals remain stable up to 260–280 °C in a wide composition range, and for the first time it is proven that they show *incongruent (peritectic)* melting. The three state diagrams show *one eutectic*, i.e. between polymer and co-crystal in case of PBTTT and PBTTT-OR-R, and between polymer and $PC_{61}BM$ for PBTTT-$(OR)_2$. The latter eutectic beyond 280 °C leads to a reversible 'solid-solid' transformation with the corresponding co-crystal. Isothermal treatments, at the onset temperature of co-crystallization during non-isothermal cooling, show no loss of co-crystal quality in combination with $PC_{61}BM$ perfectioning for fullerene-rich PBTTT:$PC_{61}BM$ and PBTTT-OR-R:$PC_{61}BM$ mixtures, whereas PBTTT-$(OR)_2$:$PC_{61}BM$, as well as Stille-polymerized PBTTT-OR-R:$PC_{61}BM$ with homocouplings, show suppression of co-crystallization with formation of separate crystals of polymer and $PC_{61}BM$. These opposing effects are explained by the state diagrams, showcasing their substantial value in selecting efficient annealing conditions.

1. Introduction

The continuous emergence of novel materials and significant improvements in device fabrication for organic optoelectronics, such as organic photovoltaics (OPVs) and photodetectors (OPDs), have made them complementary or even competitive to their inorganic counterparts.[1–4] In the bulk heterojunction active layer of OPVs and OPDs, an intermolecular charge-transfer (CT) state is formed at the interface between the conjugated electron donating (D) and electron accepting (A) organic semiconductors.[5,6] In cavity-enhanced OPDs, the direct CT light absorption can be exploited to extend the detectivity into the near-infrared (NIR).[6,7] To promote the CT absorption strength, a high interfacial contact area between D and A is required.[6] Mixing of D and A to the molecular level can be an elegant approach to maximize the interface,[8] as has been observed for several polymer:fullerene blends.[9–11] While (partial) miscibility in amorphous polymer:fullerene blends is common,[12–14] polymer:fullerene molecular mixing in crystalline domains has also been documented.[15,16] Novel conjugated donor-acceptor (push-pull) alternating copolymers show tunable semiconducting properties such as light absorption and charge transport, and physical properties such as solubility and crystallinity. Some of these conjugated polymers allow co-crystallization with fullerenes to form

molecularly mixed co-crystals by intercalation of the fullerenes in between the side chains of the polymer backbones.[16,17] These molecularly mixed co-crystals with a constant conjugated polymer:fullerene mixing ratio, also called molecular compounds and abbreviated as 'co-crystals' in the field of OPV, are thermodynamically stable by van der Waals interactions or hydrogen bonds and provide the desired high interfacial contact and CT state enhancement.[18,19] The prototype alternating polymer of this category is PBTTT (poly[2,5-bis(3-tetradecylthiophen-2-yl)thieno[3,2-*b*]thiophene]). When mixed with $PC_{71}BM$ or $PC_{61}BM$ ([6,6]-phenyl-$C_{71(61)}$-butyric acid methyl ester), the semi-crystalline PBTTT:fullerene blends show intercalated co-crystals.[16,17,20–22] PBTTT:$PC_{61}BM$ has been successfully used to produce a NIR sensor.[23]

In order to achieve a tunable wavelength range for organic NIR photodetectors and improve the CT absorption strength at even longer wavelengths, two novel variants of PBTTT were recently synthesized by the classical Stille polymerization method, replacing the two C_{14}-alkyl side chains of the PBTTT repeating unit with one or two C_{14}-alkoxy side chains and called PBTTT-OR-R and PBTTT-$(OR)_2$, respectively (as shown in Figure 1).[24] However, common side products of cross-coupling polymerization reactions are chain structural defects called homocouplings[3] (i.e. monomers reacting to themselves rather than the complementary functionalized building blocks), disturbing the desired alternating sequence of the polymer backbone.[25] It was suggested by Matrix-Assisted Laser Desorption-Ionization - Time of Flight Mass Spectrometry (MALDI-ToF MS) that the amount of homocoupling defects in the PBTTT derivatives scales with the number of alkoxy side chains, and this was confirmed and quantified by high-resolution Ultra-High Vacuum Scanning Tunneling Microscopy (UHV-STM) as PBTTT (likely < 5%) < PBTTT-OR-R (19%) < PBTTT-$(OR)_2$ (26%).[26,27] The ability for intercalation and co-crystallization with $PC_{61}BM$ is significantly influenced by the amount of homocoupling defects. While still of minor influence for PBTTT, PBTTT-OR-R clearly shows distorted (less perfect) co-crystals of lower thermal stability,[27] and the 26% of defects in PBTTT-$(OR)_2$ is too high for co-crystal formation, as indicated by Rapid Heat-Cool Differential Scanning Calorimetry (RHC) combined with X-Ray Diffraction (XRD) measurements.[26] In our recent work, the Stille cross-coupling

polymerization was replaced by an alternative oxidative polymerization method. In this case, MALDI-ToF MS and UHV-STM indicated that homocoupling-free PBTTT derivatives were obtained.[26,27] It was further clearly proven by RHC and temperature-resolved synchrotron XRD that these homocoupling-free polymers PBTTT, PBTTT-OR-R, and PBTTT-$(OR)_2$ form intercalated co-crystals with $PC_{61}BM$ in a 1:1 molar mixing ratio (ca. 45:55 w/w% mixing ratio; see Figure 1). Note that regiochemical irregularities in case of dissimilar side groups in the repeating unit, i.e. in case of PBTTT-OR-R, can be regarded as an extra chain 'defect'. However, this extra type of irregularity has no (or a very limited) effect on co-crystallization and PBTTT-OR-R:$PC_{61}BM$ co-crystal properties.[27]

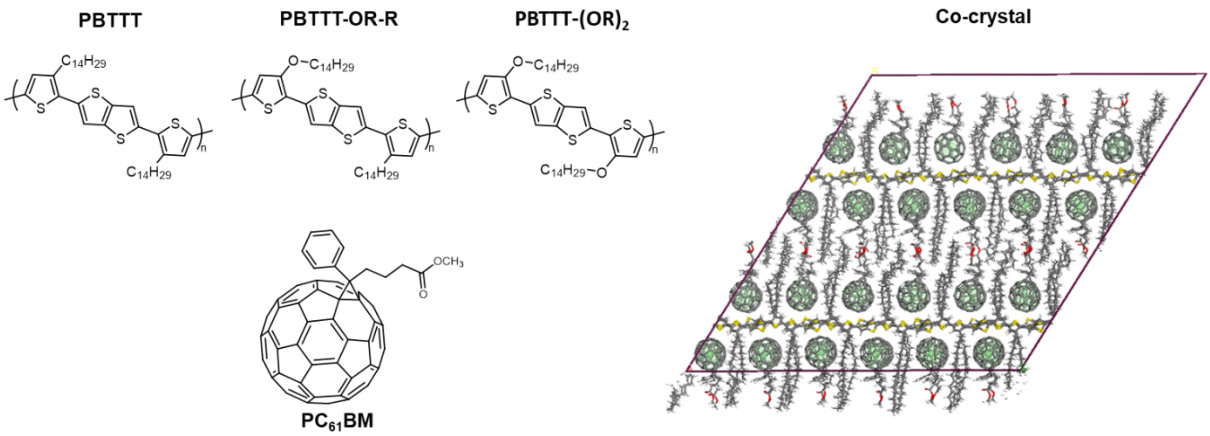

Figure 1. Repeating units of PBTTT, PBTTT-OR-R, and PBTTT-$(OR)_2$, and structure of $PC_{61}BM$. Schematic representation of co-crystal formation in PBTTT:$PC_{61}BM$ (1:1 molar mixing ratio), reproduced with permission from [26].

Although the true structure of alternating conjugated polymers might deviate from the idealized picture of the repeating unit in many occasions, this issue received relatively limited attention up to now. Nevertheless, synthesis routes toward defect-free alternating conjugated polymers, giving rise to defect-free co-crystals in their mixtures with fullerenes, are most likely of importance for (opto)electronic applications with improved performance. This has been illustrated by the enhanced CT absorption of PBTTT-$(OR)_2$:$PC_{61}BM$ (20:80 w/w%) photodiodes (measured by their external quantum efficiency (EQE)) in comparison with devices based on active layers with homocoupling defects.[24,26] Another example is the different effect of thermal annealing on the stability of the intercalated morphology of PBTTT-OR-R:$PC_{61}BM$ (20:80 w/w%) active layers with or without

homocoupling defects (also demonstrated by EQE analysis).[27] Also, from a more general scientific point of view, the availability of defect-free alternating conjugated polymers is utmost important to establish reliable phase (state) diagrams of their mixtures with fullerenes. In general, the phase diagrams of conjugated polymer:fullerene mixtures (blends) are important to understand the role of all occurring phases and morphologies as a function of mixture composition and temperature and help in designing optimized properties of the active layers in organic optoelectronic devices. This rational methodology is in contrast with a trial and error approach after fabrication of devices which is often lacking deeper insight in the working mechanism of the considered polymer:fullerene system.

'Phase' diagrams involving polymers and other high molar mass components (e.g. fullerenes) are rather 'state' diagrams than phase diagrams because equilibrium conditions of liquidus and solidus lines are mostly not reached. This is the result of kinetic effects during the applied processing and characterization, such as effects of cooling and heating rates, supercooling, reorganization, and isothermal vs. non-isothermal pathways. Instead of purely crystalline phases from the constituents and eutectics, amorphous phases are also interfering. The glass transition temperatures of these amorphous phases might lead to vitrification effects, also at the eutectic composition.[28,29] Despite their added value to reveal composition-temperature-morphology relationships, state (phase) diagrams of conjugated polymer:fullerene systems are scarce in literature.[10,21,28–32] In case of co-crystal formation, the classical binary state diagram turns into a double binary state diagram, i.e. one between conjugated polymer and co-crystal and one between co-crystal and fullerene. To the best of our knowledge, only two alternating conjugated polymer:fullerene state diagrams are published in literature, both for PBTTT, but synthesized by Stille cross-coupling polymerization (hence containing homocoupling defects), and mixed with the fullerenes $PC_{71}BM$[31] and $PC_{61}BM$.[21]

In this paper, a wide range of mixture compositions are studied by means of RHC and T-resolved synchrotron XRD to establish the state diagrams of PBTTT:$PC_{61}BM$, PBTTT-OR-R:$PC_{61}BM$, and PBTTT-$(OR)_2$:$PC_{61}BM$. Importantly, and different from all previous studies, homocoupling-free alternating conjugated polymers are used, synthesized by oxidative polymerization, ensuring the correct

molecular structure to allow co-crystal formation in all systems studied. The melting temperature of homocoupling-free PBTTT, PBTTT-OR-R, and PBTTT-$(OR)_2$ is increasing with alkoxy substitution, while for the co-crystals the melting transition is highest for the PBTTT:$PC_{61}BM$ co-crystal. This change of relative values between polymer and corresponding co-crystal leads to changes in their state diagrams, allowing for the first time a systematic study of occurring similarities and differences. All state diagrams show one eutectic, between polymer and co-crystal in case of PBTTT and PBTTT-OR-R, and between polymer and $PC_{61}BM$ for PBTTT-$(OR)_2$. Special attention is paid to the melting behavior of all components. While the alternating polymers, $PC_{61}BM$, and the eutectics melt congruently, all co-crystals show *incongruent (peritectic) melting*. The experimental data are qualitatively compared to calculations based on the Flory-Huggins theory for the liquid mixture state and standard thermodynamic models for the crystalline state of the pure components and the co-crystal. Finally, a comparison is made with classical Stille-polymerized PBTTT-OR-R to showcase the effect of homocoupling defects on the state diagram and efficient isothermal treatments.

2. Results and discussion

The thermal behavior of the homocoupling-free neat conjugated polymers PBTTT, PBTTT-OR-R, and PBTTT-$(OR)_2$ and their pure co-crystals with $PC_{61}BM$ has been described before by means of RHC in combination with temperature-resolved synchrotron XRD.[26,27] By mixing the homocoupling-free PBTTT derivatives with $PC_{61}BM$, a co-crystal is always formed of which the polymer:$PC_{61}BM$ mixing ratio was confirmed to be 45:55 w/w% for the three pure co-crystals, i.e. a ratio close to the 1:1 molar ratio of the polymer repeating units and $PC_{61}BM$ (see Figure 1). Both RHC and T-resolved XRD show that the co-crystals of each system have a different melting/crystallization transition compared to the pure polymer and $PC_{61}BM$. The endset temperature, denoted as $T_{m,endset}$, of the melting trajectory and of the T-resolved diffraction peak in heating of the PBTTT co-crystal is slightly higher than that of pure PBTTT, while $T_{m,endset}$ for both co-crystals of PBTTT-OR-R and PBTTT-$(OR)_2$ is lower than that of the respective pristine alternating polymers.[26,27] These relative changes in $T_{m,endset}$ are illustrated in the RHC thermograms of Figure S1.

Thermal stability of the pure components

The thermal stability of PBTTT, PBTTT-OR-R, and PBTTT-$(OR)_2$ was investigated using Thermogravimetric Analysis (TGA) (Figure S2) to ensure reliable thermal treatments in RHC and XRD. Especially the temperature and time duration above the melting transition of all components is crucial for a reproducible subsequent cooling and 2nd heating. Considering the onset temperature of mass loss in an inert nitrogen atmosphere (T_{deg}) as a measure to compare the thermal stability of the three conjugated polymers, it is clear from Figure S2 that PBTTT is most stable, with T_{deg} > 400 °C, and PBTTT-$(OR)_2$ is least stable, i.e. $T_{deg.}$ of PBTTT > PBTTT-OR-R > PBTTT-$(OR)_2$. Therefore, the maximum temperature in the melt was limited to 320 °C for 1 minute during the XRD analysis for all systems to avoid thermal degradation effects. A temperature of 330 °C was permitted during RHC analysis but here the residence time was limited to 0.1 minute.

State diagrams of PBTTT:$PC_{61}BM$, PBTT-OR-R:$PC_{61}BM$, and PBTTT-$(OR)_2$:$PC_{61}BM$ by means of RHC and T-resolved synchrotron XRD

Besides the pure polymers and the pure co-crystals, a variety of mixtures for each of the three polymer:$PC_{61}BM$ systems was analyzed here. The chosen compositions cover polymer-rich as well as fullerene-rich mixtures to enable a systematic investigation of the phase behavior around the 45:55 w/w% co-crystal composition and to establish the respective state diagrams by the combined information of RHC and T-resolved synchrotron XRD. The RHC and XRD data sets are complementary for the construction and interpretation of reliable state diagrams. The XRD data give detailed structure information in case of overlapping RHC melting peaks. The structure corresponding to $T_{m,endset}$ of such overlapping RHC peaks was determined by comparison with the T-resolved diffraction peaks of the same polymer:$PC_{61}BM$ composition. The RHC second heating thermograms (at 500 K min^{-1}) for all compositions of the three polymer:$PC_{61}BM$ systems are grouped in Figure 2 (a-c) with the weight ratio indicated on the right of each thermogram. The preceding slow cooling thermograms at 20 K min^{-1} are shown in Figure S3. The signal to noise ratio of these slow cooling thermograms is limited, hindering accurate characterization, especially for some polymer-rich mixtures of PBTTT-OR-R:$PC_{61}BM$ and

PBTTT-$(OR)_2$:$PC_{61}BM$. Therefore, a faster RHC cooling rate of 500 K min^{-1} was also applied (Figure S4) to investigate transitions, the onset temperature of crystallization $T_{c,onset}$ of polymer backbones and co-crystals, and supercooling in a more accurate way. The supercooling is calculated here as $T_{m,endset}$ - $T_{c,onset}$. Note that the first heating prior to the cooling from the melt is not shown as it depends on the poorly defined preceding solution processing of the material, and generally leads to less reproducible results which are not suited for the construction of a reliable state diagram. In order to construct the state diagrams with focus on the liquidus lines of the different phases, the RHC melting trajectories and the T-resolved diffraction peaks are characterized by the $T_{m,endset}$ of the polymer backbones, co-crystals, and $PC_{61}BM$. $T_{m,onset}$ symbols are not indicated on the RHC thermograms of Figure 2 and these values were not used for the construction of the solidus lines in the state diagrams. The determination of $T_{m,onset}$ is less accurate because of clear thermal reorganization of the co-crystals during melting, even upon heating at 500 K min^{-1}, and noticed as dual co-crystal melting peaks in the RHC thermograms. This reorganization upon heating indicates that the crystals formed during cooling are not yet perfect and will still evolve towards a more stable structure in the subsequent heating. The shape of the dual melting peak depends on the preceding cooling, which is illustrated by the RHC thermograms for a fast heating at 500 K min^{-1} (Figure S5) applied to the same mixtures of the three polymer:$PC_{61}BM$ systems as in Figure 2, but after a fast cooling at 500 K min^{-1} (Figure S4). The dual or bimodal shape of the co-crystal melting peaks in Figure S5 is much less pronounced than in Figure 2 and more smeared out, starting from lower temperatures, as a result of the formation of less perfect crystals during faster cooling. Besides melting of the polymer backbones, the co-crystals, and $PC_{61}BM$, also side chain melting of the conjugated polymers is observed in Figure 2, at the lower temperature side, for polymer-rich mixtures up to around 70:30 w/w% mixing ratio (the crystallization of the side chains of the polymer-rich mixtures is also seen in Figure S3 and S4). The side chain melting transition is more complicated with a double peak up to 150 °C in case of PBTTT.[33] Side chain melting is absent for mixtures in which the polymer is completely incorporated in the co-crystal, as also seen before.[26,27] After side chain melting, the conjugated polymers are in a liquid crystalline state with a *mobile* amorphous side chain fraction, and finally turn into the fully molten state after complete backbone disordering at the higher

temperature side ('backbone melting'). For the construction of the state diagrams, side chain melting is not further considered.

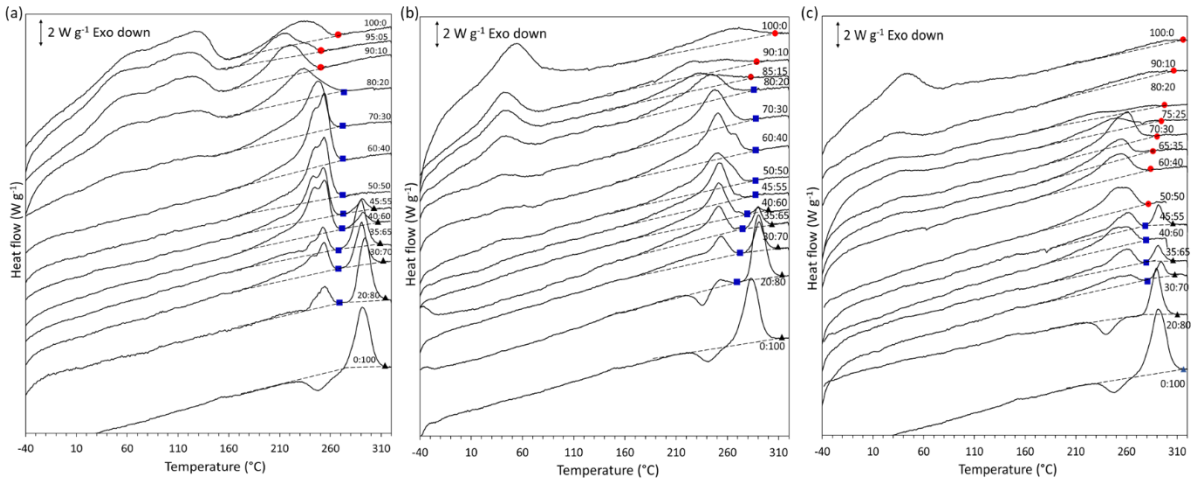

Figure 2. RHC heating curves at 500 K min^{-1} after cooling from the melt at 20 K min^{-1} for (a) PBTTT:$PC_{61}BM$, (b) PBTTT-OR-R:$PC_{61}BM$, and (c) PBTTT-$(OR)_2$:$PC_{61}BM$ mixtures. The closed red circles, blue squares, and black triangles represent $T_{m,endset}$ of the melting peak for the polymer backbones, co-crystals, and $PC_{61}BM$, respectively. Curves are vertically shifted for clarity.

Plotting the experimental $T_{m,endset}$ data points of the RHC thermograms of Figure 2 (a-c) and the endset values of the T-resolved diffraction peaks as a function of the $PC_{61}BM$ content (in w%), the liquidus lines of the respective PBTTT derivatives (red circles), $PC_{61}BM$ (black triangles), and the corresponding co-crystals (blue squares) are obtained, representing the respective state diagrams of PBTTT:$PC_{61}BM$ in Figure 3 (a,d), PBTTT-OR-R:$PC_{61}BM$ in Figure 3 (b,e), and PBTTT-$(OR)_2$:$PC_{61}BM$ in Figure 3 (c,f). The upper row of Figure 3 represents the RHC data, the middle row the XRD data, and the lower row is a schematical representation of the three calculated phase diagrams using the seminal Flory-Huggins

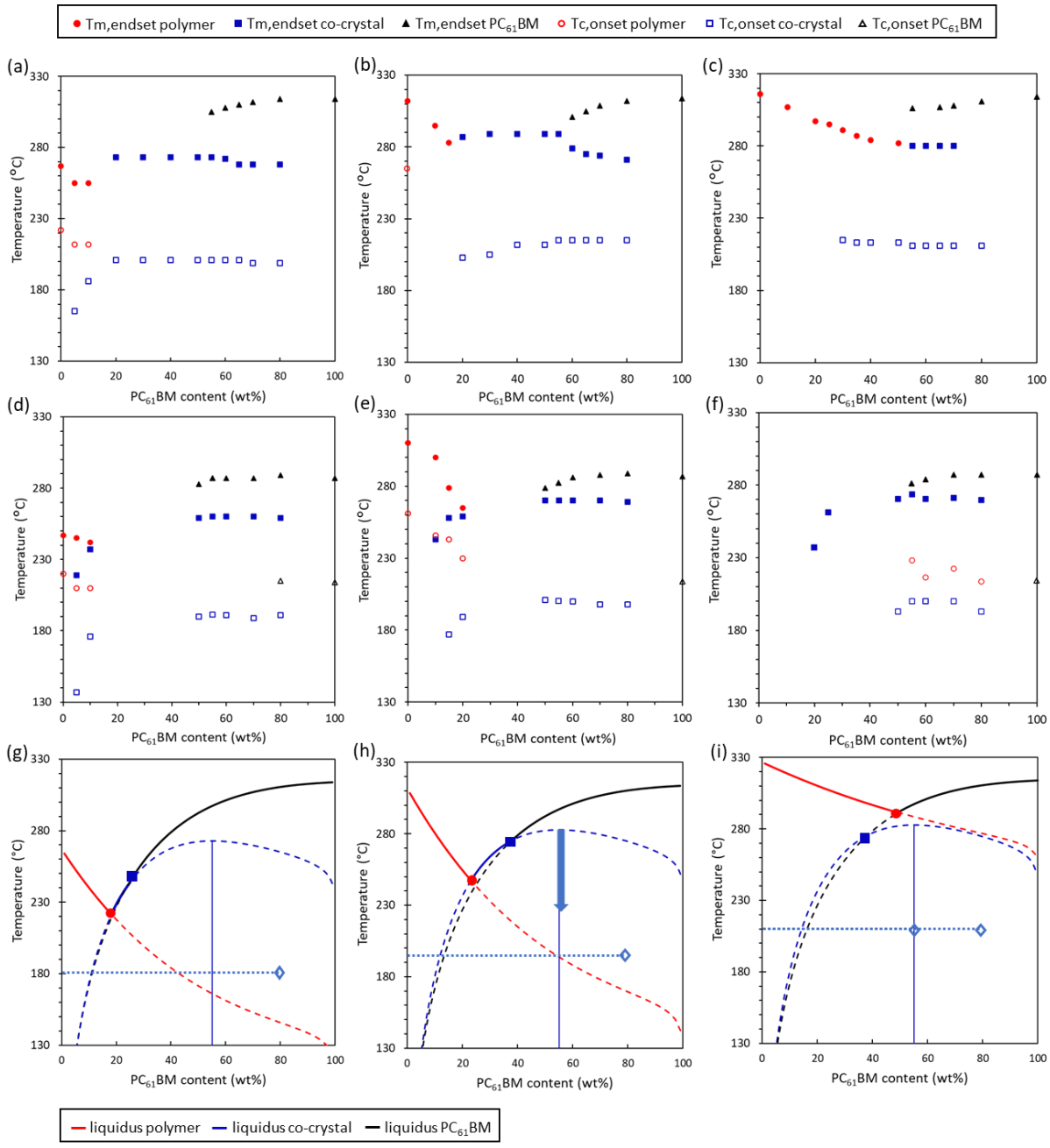

Figure 3. Upper row: State diagrams based on $T_{m,endset}$ values from the RHC thermograms of Figure 2: (a) PBTTT:$PC_{61}BM$, (b) PBTTT-OR-R:$PC_{61}BM$, and (c) PBTTT-$(OR)_2$:$PC_{61}BM$. Middle row: State diagrams based on endset values of T-resolved XRD: (d) PBTTT:$PC_{61}BM$, (e) PBTTT-OR-R:$PC_{61}BM$, and (f) PBTTT-$(OR)_2$:$PC_{61}BM$. $T_{m,endset}$ values for the polymer backbones, co-crystals, and $PC_{61}BM$ are indicated with red circles, blue squares, and black triangles (full symbols), respectively. Open symbols indicate onset values of crystallization $T_{c,onset}$ in cooling. Lower row: Schematic calculated phase diagrams for (g) PBTTT:$PC_{61}BM$, (h) PBTTT-OR-R:$PC_{61}BM$, and (i) PBTTT-$(OR)_2$:$PC_{61}BM$ with incongruently melting co-crystals. The liquidus lines are indicated in red for the polymers, in blue for the co-crystals, and in black for $PC_{61}BM$, respectively. The full lines indicate the thermodynamically stable states and the dashed lines are thermodynamically metastable states that possibly could be reached in dynamic measurement conditions for kinetic reasons. Eutectic and peritectic compositions are indicated by a red circle and blue square, respectively. The pure co-crystals at 55 w% $PC_{61}BM$ are indicated as thin blue vertical lines. The isothermal crystallization temperatures (horizontal dotted lines) and the chosen mixture compositions (open blue symbols) are indicated (for more details, see § Isothermal treatments). The blue arrow in (h) indicates the relative downward shift of the co-crystal liquidus line

against the liquidus lines of PBTTT-OR-R and $PC_{61}BM$ in case of homocoupling defects in the Stille-polymerized PBTTT-OR-R (for more details, see § Homocoupling defects).

theory for the liquid mixture state and standard thermodynamic models for the crystalline state of the pure components and the co-crystals.

More intermediate mixture compositions and a reliable melting point depression could be studied by RHC, especially in case of PBTTT-$(OR)_2$:$PC_{61}BM$ mixtures, as shown in Figure 3 (c). PBTTT-$(OR)_2$ has a melting temperature beyond the upper temperature limit of the XRD measurement (320 °C) and shows a clear thermal degradation before being fully molten. The value of $T_{m,endset}$ for pure PBTTT-$(OR)_2$ is therefore unreliable and the further melting point depression not measurable with the XRD set-up (Figure 3 (f)). The onsets of crystallization from the RHC thermograms of Figure S3 and the XRD synchrotron measurements in cooling at 20 K min^{-1} are also indicated in Figure 3 (a-c) and Figure 3 (d-f) (open symbols). Both RHC and XRD data sets are in good agreement, except for the absolute temperature assignment for which a systematically higher value of ca. 15 °C is noticed for RHC than for XRD, partly due to the 10-fold higher heating rate of RHC, but also possibly due to differences in sensitivity or the less accurate calibration conditions of the Linkam hot-stage sample set-up in XRD.

Some general features are noticed in the three state diagrams, which are made clear by the calculated liquidus lines in the lower row of Figure 3. More details on the calculations are given in the Supporting Information. While the upper and middle row of Figure 3 represent state diagrams, depending on experimental conditions (kinetics of transformations), the lower row represents equilibrium phase diagrams, with stable (full) and metastable (dashed) parts of the liquidus lines. For polymer-rich mixtures, a depression of $T_{m,endset}$ of the polymer backbone melting can be seen (closed red circles and solid red lines in calculated phase diagrams). When the $PC_{61}BM$ content is further increased, $T_{m,endset}$ increases again to a value corresponding to $T_{m,endset}$ of the pure co-crystal melting at 45:55 w/w% (closed blue squares). Intermediate compositions between 0 and 55 w% of $PC_{61}BM$ reveal a eutectic. When the $PC_{61}BM$ content exceeds 50 w%, a $PC_{61}BM$ melting peak follows the co-crystal melting peak (black closed triangles and solid black lines in calculated phase diagrams), which is an indication of the *incongruent* melting of the co-crystals (*vide infra*).

Note that the co-crystals are formed with a supercooling of 70 °C or more if cooled at 20 K min^{-1} (compare open and closed blue squares in Figure 3), and even up to 100 °C or more if cooled at 500 K min^{-1}. The supercooling for the backbone crystallization of the pure polymers and the polymer-rich mixtures is much lower (around 35–45 °C, compare open and closed red circles in Figure 3). All co-crystals remain stable up to high temperatures (260–280 °C) over a wide polymer:$PC_{61}BM$ mixing range, as indicated by the melting temperatures $T_{m,endset}$ for RHC and XRD in Figure 3 (blue squares), close to the value for the pure co-crystal (45:55 w/w% mixing ratio) and as a consequence leading to rather flat liquidus lines.

In Figure 4, the evolution of the *total* melting enthalpy ΔH_m of the three systems (black symbols) was calculated from Figure 2 as a function of the mixtures' $PC_{61}BM$ content (in J per g of mixture), and compared to the polymer *backbone/co-crystal* melting enthalpy (red symbols). The total melting enthalpy of a mixture includes, besides the melting of the backbone of the polymer and/or the melting of the corresponding co-crystal, also the melting of the side chains and $PC_{61}BM$ along the RHC trajectory. Figure 4 shows that this total melting enthalpy is highest for the pure polymer and is continuously decreasing with $PC_{61}BM$ content, irrespective the preceding RHC cooling (compare the trend of ΔH_m after slow cooling (left column) and fast cooling (right column)). This decreasing evolution of ΔH_m means that the reduction in side chain melting enthalpy of the polymer is not compensated by the incorporation of $PC_{61}BM$ in the co-crystal. Figure 4 also shows that the polymer backbone/co-crystal melting enthalpy goes through a maximum with increasing $PC_{61}BM$ content, indicating that the co-crystal has a significantly higher melting enthalpy than the corresponding pure polymer backbone, in agreement with literature.[17]

Besides these general features, the changes in the $T_{m,endset}$ values of the pure polymers and to a lesser extent of the pure co-crystals lead to differences in (i) the composition and temperature of the eutectic between polymer and co-crystal (crossing of red and blue liquidus lines in case of PBTTT:$PC_{61}BM$ and PBTTT-OR-R:$PC_{61}BM$; Figure 3 (g,h)) or between polymer and $PC_{61}BM$ (crossing of red and black liquidus lines in case of PBTTT-$(OR)_2$:$PC_{61}BM$; Figure 3 (i)), and (ii) the mixture composition which starts showing

the additional melting peak of $PC_{61}BM$ (crossing of blue and black liquidus lines; Figure 3 (g-i)). Note that if the RHC state diagrams were constructed based on $T_{m,endset}$ values of Figure S5 (after a fast cooling at 500 K min^{-1}, see Figure S4), the same general features and differences between the three state diagrams of Figure 3 remain valid, as shown in Figure S6.

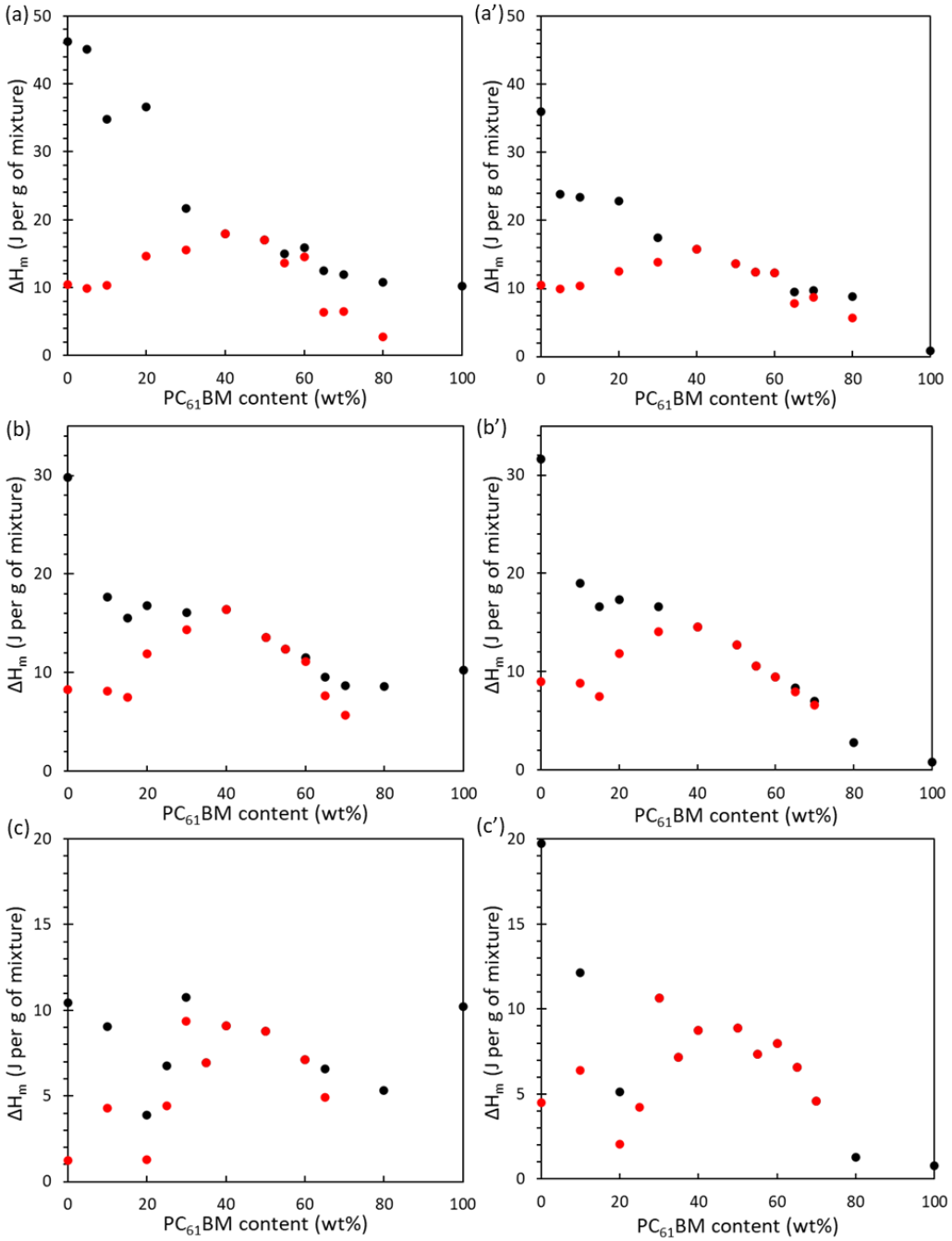

Figure 4. Total (black) and polymer backbone/co-crystals (red) melting enthalpy for mixtures of (a, a') PBTTT:$PC_{61}BM$, (b, b') PBTTT-OR-R:$PC_{61}BM$, and (c, c') PBTTT-$(OR)_2$:$PC_{61}BM$, calculated in J per g of mixture from the RHC results of Figure 2 (cooling at 20 K min^{-1}; a, b, c) and of Figure S5 (cooling at 500 K min^{-1}; a', b', c').

Eutectic between polymer and co-crystal for PBTTT:$PC_{61}BM$ and PBTTT-OR-R:$PC_{61}BM$

At the polymer-rich side in Figure 3 (a,d), it is seen that the intersection of the liquidus line of PBTTT with that of the co-crystal appears around a mixing ratio PBTTT:$PC_{61}BM$ of 90:10 w/w%, giving a eutectic between PBTTT and its co-crystal. PBTTT-OR-R:$PC_{61}BM$ shows a similar eutectic at a slightly higher $PC_{61}BM$ content (at least 15 w% $PC_{61}BM$) and at a temperature closer to $T_{m,endset}$ of its co-crystal, as seen in Figure 3 (b,e). The eutectic of the two systems is clearly proven by the T-resolved synchrotron Small Angle X-ray Scattering (SAXS) results of their polymer-rich mixtures, as demonstrated in Figure 5 (a,b). Figure 5 (a) exhibits two diffractions at q = 0.208 $Å^{-1}$ and q= 0.281 $Å^{-1}$ (d-spacing of 30.2 Å and 22.4 Å) in the SAXS pattern of the 90:10 w/w% mixture of PBTTT:$PC_{61}BM$ from room temperature, corresponding to the co-crystal and PBTTT, respectively. It can be seen that the two diffractions evolve with temperature, as explained in our previous work,[26,27] and disappear around the same temperature of 230 °C, which is lower than the melting temperatures of pure PBTTT and co-crystal.

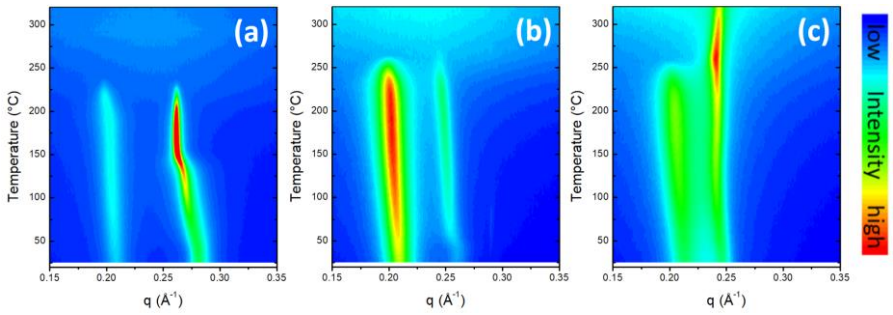

Figure 5. Temperature-resolved synchrotron SAXS heating patterns of polymer-rich mixtures of (a) PBTTT:$PC_{61}BM$ in a 90:10 w/w% mixing ratio, (b) PBTTT-OR-R:$PC_{61}BM$ in a 80:20 w/w% mixing ratio, and (c) PBTTT-$(OR)_2$:$PC_{61}BM$ in a 75:25 w/w% mixing ratio. Heating at 50 K min^{-1} from 25 °C to 320 °C by Linkam hot-stage after cooling at 20 K min^{-1} from 320 °C to -50 °C in RHC. The color scale bar is indicative for the relative increasing intensity of the diffraction patterns (from blue to red).

Figure 5 (b) shows the 80:20 w/w% mixture of PBTTT-OR-R:$PC_{61}BM$ with a similar T-resolved SAXS result upon heating. The co-crystal reflection occurs at the same q- value as for PBTTT based co-crystals whereas the PBTTT-OR-R polymer reflection has shifted to a lower q-value compared to PBTTT,

indicating a larger layer stack periodicity for crystallized PBTTT-OR-R polymer.[27] The $T_{m,endset}$ values (close to the eutectic temperature) are higher than in Figure 5 (a) (260 °C), but again lower than for pure PBTTT-OR-R and the corresponding co-crystal. The eutectics of the two systems are slightly different due to the presence of alkoxy side groups in PBTTT-OR-R, increasing $T_{m,endset}$ of the backbone melting, while the $T_{m,endset}$ values of the respective co-crystals remain much closer to each other.[26,27] As indicated in the schematic phase diagrams of Figure 3, the (red) liquidus line of PBTTT (Figure 3 (g)) shifts to higher temperatures for PBTTT-OR-R (Figure 3 (h)). As a result, the intersection of the liquidus line of PBTTT-OR-R and the (blue) liquidus line of the co-crystal occurs at a higher $PC_{61}BM$ content and at a higher temperature than for PBTTT. Interestingly, the supercooling becomes smaller than for the pure polymer when reaching the eutectic composition in both PBTTT:$PC_{61}BM$ and PBTTT-OR-R:$PC_{61}BM$, which might be caused by an increasing nucleation density of the concurrent crystallization of polymer and co-crystal phases in the vicinity of the eutectic composition.

The absence of a eutectic between PBTTT-$(OR)_2$ and its co-crystal at low $PC_{61}BM$ content is illustrated by the SAXS pattern of the PBTTT-$(OR)_2$:$PC_{61}BM$ mixture in a 75:25 w/w% ratio in Figure 5 (c). The reflections of both co-crystal and PBTTT-$(OR)_2$ are seen at room temperature, but the co-crystal signal melts at around 260 °C, while the PBTTT-$(OR)_2$ crystal reflection becomes significantly stronger beyond 260 °C by extra crystallization and remains crystalline until the upper temperature limit of the measurement. The appearance of a eutectic in the PBTTT-$(OR)_2$:$PC_{61}BM$ system beyond 280 °C is discussed in more detail below.

Incongruent co-crystal melting for $PC_{61}BM$-rich compositions

A two-component system forming co-crystals can in general show a different type of phase diagram depending on the *congruent* or *incongruent* melting behavior of the co-crystals, as illustrated in the theoretical phase diagrams of Figure S7.[18,19,34] In the specific case of PBTTT (and derivatives) with $PC_{61}BM$, the respective state diagrams involve *incongruent melting of the co-crystals*. The liquidus line of the co-crystals intersects with the liquidus line of $PC_{61}BM$ at a composition richer in polymer than the pure co-crystal composition (45:55 w/w% mixing ratio), as observed for each system in Figure 3

(lower row, see crossing of blue and black liquidus lines). For higher $PC_{61}BM$ contents, exceeding the content at the intersection point, the melting of co-crystals would form a mixed liquid and a solid $PC_{61}BM$ phase. This is highlighted with the T-resolved synchrotron Small Angle/Wide Angle X-ray Scattering (SAXS/WAXS) patterns of Figure 6 for a 45:55 w/w% (pure co-crystal) and 20:80 w/w% mixing ratio of the three systems.

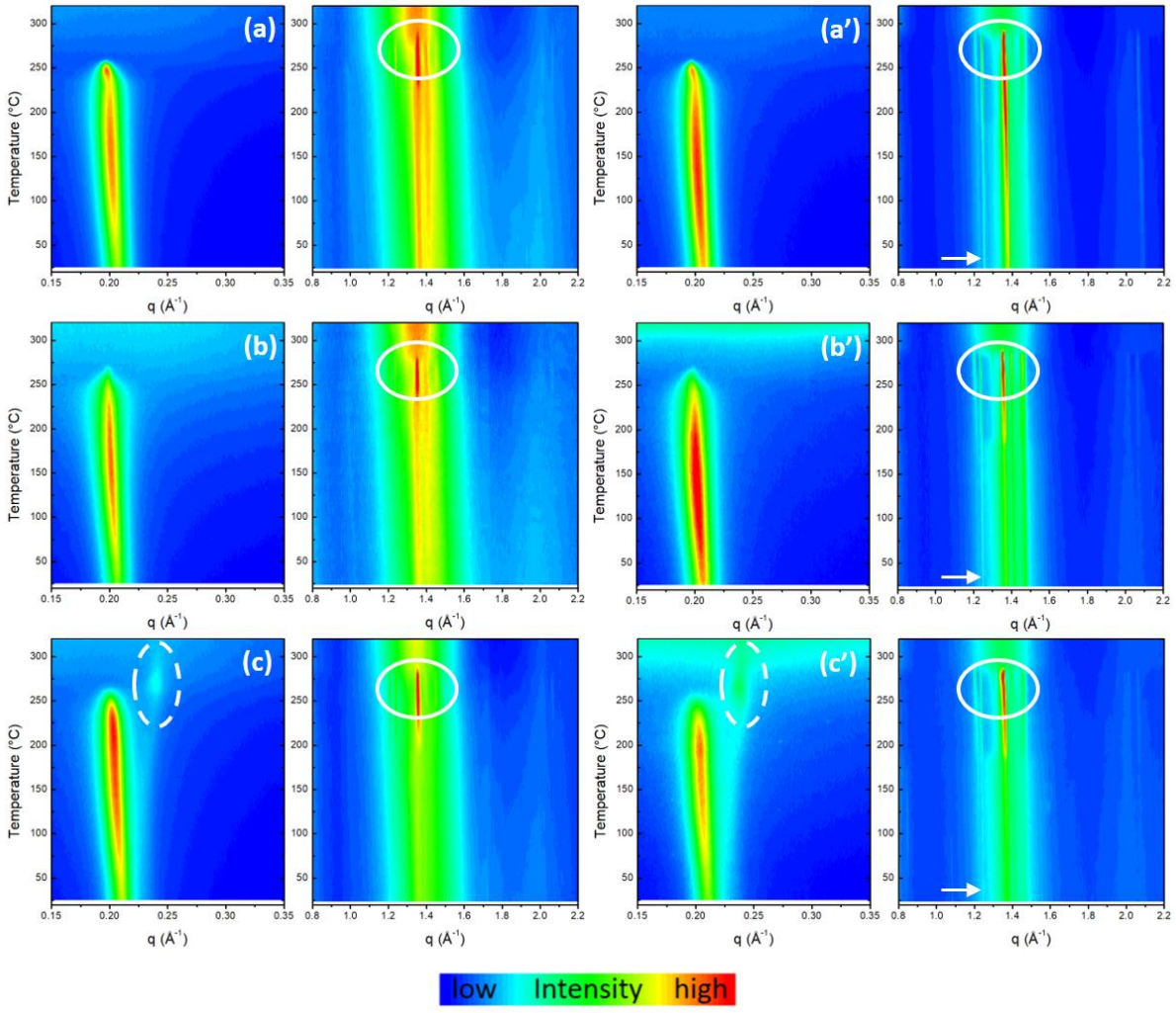

Figure 6. Temperature-resolved synchrotron SAXS and WAXS heating patterns of $PC_{61}BM$-rich mixtures of (a,a') PBTTT:$PC_{61}BM$, (b,b') PBTTT-OR-R:$PC_{61}BM$, and (c,c') PBTTT-$(OR)_2$:$PC_{61}BM$ in a 45:55 w/w% (a,b,c) and 20:80 w/w% (a',b',c') mixing ratio. Heating at 50 K min^{-1} from 25 °C to 320 °C by Linkam hot-stage after cooling at 20 K min^{-1} from 320 °C to -50 °C in RHC. The color scale bar is indicative for the relative increasing intensity of the diffraction patterns (from blue to red). The circled high-temperature reflections in the WAXS patterns are due to $PC_{61}BM$ crystals. The dashed-circled high-temperature reflection in the SAXS panel of (c,c') relates to pure PBTTT-$(OR)_2$ crystals. The arrows in (a',b',c') indicate excess $PC_{61}BM$ at 25 °C.

As shown in the SAXS patterns during heating in Figure 6, the respective co-crystal diffractions of 45:55 w/w% mixtures (q-values around 0.21 $Å^{-1}$) are seen from 25 °C and disappear around 260 °C, indicating a melting of the co-crystals, while above the end of this melting, multiple reflections appear in the WAXS patterns due to $PC_{61}BM$ crystallization and final melting. At an even higher $PC_{61}BM$ content, similar results can be seen. Figure 6 (right) shows T-resolved SAXS and WAXS results of the 20:80 w/w% mixtures which show that, beyond the end of co-crystal melting, the $PC_{61}BM$ reflections of each mixture become more intense around 265 °C. The only difference between the two compositions is that the 20:80 w/w% mixtures present excess $PC_{61}BM$, indicated by arrows in Figure 6, which either crystallized during the previous cooling (mainly in the case of PBTTT:$PC_{61}BM$) and/or underwent cold crystallization during heating (mainly in the case of PBTTT-OR-R:$PC_{61}BM$ and PBTTT-$(OR)_2$:$PC_{61}BM$). Thus, both T-resolved SAXS/WAXS results prove that incongruent melting of co-crystals leads to solid $PC_{61}BM$ for the three systems. It is important to note that kinetics are not only important for reorganization effects but also play a significant role on the incongruent melting behavior of the co-crystals. As an example, in Figure S8, the effect of different cooling rates is shown on the reorganization and incongruent melting with formation of $PC_{61}BM$ for pure co-crystals of PBTTT:$PC_{61}BM$ (45:55 w/w% composition). It illustrates that state diagrams are not unique for a particular system, but can vary with applied process conditions.

In conclusion, besides one eutectic transition on the polymer-rich side, the PBTTT:$PC_{61}BM$ and PBTTT-OR-R:$PC_{61}BM$ systems both show *incongruent melting* of the co-crystals and one *peritectic transition* on the $PC_{61}BM$-rich side. In literature, on the contrary, a double eutectic state diagram was suggested for PBTTT:$PC_{61}BM$, with the first eutectic between PBTTT and the co-crystal around 10 w% $PC_{61}BM$, and the second eutectic between the co-crystal and $PC_{61}BM$ at 43 w% $PC_{61}BM$. The pure co-crystal composition, in between the two eutectics, was considered at 40 w% $PC_{61}BM$ because of the detection of a pure $PC_{61}BM$ phase starting at mixture compositions from around 40 w% $PC_{61}BM$.[21] Note that this co-crystal composition is not corresponding to a PBTTT:$PC_{61}BM$ 1:1 molar mixing ratio, and the co-crystal was assumed to melt *congruently.*

Eutectic between PBTTT-(OR)$_2$ and PC$_{61}$BM beyond 280 °C

If $T_{m,endset}$ of the polymer backbone melting further shifts to higher temperatures, as indicated for PBTTT-(OR)$_2$ in Figure 3 (i), the liquidus lines of the polymer and PC$_{61}$BM will intersect above the liquidus line of the co-crystal. In this case, the polymer will form a eutectic with PC$_{61}$BM at a temperature above $T_{m,endset}$ (around 260 °C) of the pure co-crystal, i.e. beyond 280 °C. Note that the liquidus line of the co-crystal in Figure 3 (f) is stable over a wide composition range *below* the eutectic temperature, as was already noticed for the other systems in Figure 3 (d,e). In cooling PC$_{61}$BM-rich mixtures of PBTTT-(OR)$_2$:PC$_{61}$BM (at 20 K min^{-1} from 320 °C to 25 °C), the PBTTT-(OR)$_2$ backbone is crystallizing first (with a low supercooling of less than 40 °C), which leads to layered liquid crystalline matter with a characteristic SAXS reflection as indicated with a white arrow in Figure 7 for five compositions between 50 and 80 w% of PC$_{61}$BM. Subsequently, this liquid crystalline PBTTT-(OR)$_2$ is remarkably 'transformed' into the more stable co-crystal which starts crystallizing at a temperature at which the liquid crystalline polymer has completely disappeared (and before the liquid crystalline polymer layers can be locked in by side chain crystallization). The co-crystal is formed with a supercooling of 70 °C and stays stable in a subsequent heating from 25 °C up to elevated temperatures and in a wide composition range, as can be seen in the XRD data of Figure 3 (f). The co-crystals not only lead to PC$_{61}$BM crystals by incongruent melting during (re)heating but also liquid crystalline PBTTT-(OR)$_2$ (q-values of 0.24 Å^{-1}), as shown in the SAXS patterns of Figure 6 (c). The presence of these PBTTT-(OR)$_2$ liquid crystals is related to the eutectic between PBTTT-(OR)$_2$ and PC$_{61}$BM beyond 280 °C. Taking into account the differences in supercooling between polymer backbone and PC$_{61}$BM crystallization, the transformation of polymer liquid crystal into co-crystal during cooling and the reformation of liquid crystalline polymer and PC$_{61}$BM crystals out of co-crystal during heating seems a reversible

transformation. The fast intercalation of $PC_{61}BM$ inside the *mobile side chain fraction* of the liquid crystalline PBTTT-$(OR)_2$, which is preventing the final side chain crystallization at lower temperatures, seems crucial for this apparent polymer-co-crystal 'solid-solid' transformation during cooling. As the liquid crystalline nature of the polymer is not included in the simplified Flory-Huggins calculation model, this transformation and the stability of the co-crystal cannot be explained, as seen by the equilibrium liquidus lines of Figure 3 (i). The co-crystal only appears as a metastable phase for all compositions in this calculated phase diagram. Note that in $PC_{61}BM$-rich mixtures of PBTTT:$PC_{61}BM$ and PBTTT-OR-R:$PC_{61}BM$, no preceding crystallization of the respective polymers is observed during cooling (compare the three systems in Figure S9), nor formation of polymer crystals as a result of the incongruent melting of the co-crystals during heating (see Figure 6 (a,b)).

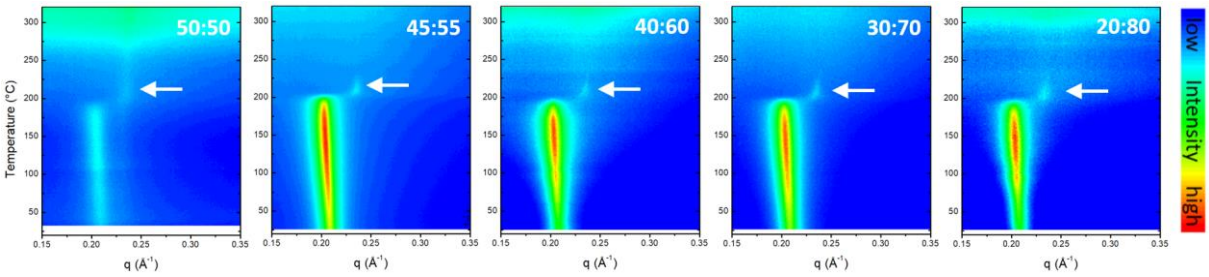

Figure 7. Temperature-resolved synchrotron SAXS cooling patterns of $PC_{61}BM$-rich mixtures of PBTTT-$(OR)_2$:$PC_{61}BM$ for five compositions between 50 and 80 w% of $PC_{61}BM$. Cooling at 20 K min^{-1} from 320 °C to 25 °C, immediately after heating from 25 °C to 320 °C at 50 K min^{-1} by a Linkam hot-stage. The color scale bar is indicative for the relative increasing intensity of the diffraction patterns (from blue to red). The white arrows indicate reflections of the crystallization of PBTTT-$(OR)_2$ before the onset of crystallization of the corresponding co-crystal.

Isothermal treatments – From state diagrams towards optoelectronic applications

The main purpose of this paper was to establish the state diagrams of three model systems of homocoupling-free alternating conjugated polymers mixed with $PC_{61}BM$ and to highlight the complexity of these 'double binary' diagrams by the interference of incongruently melting co-crystals formed as a third component with a polymer:$PC_{61}BM$ composition of 45:55 w/w%. These state diagrams can be a valuable tool for guiding the morphological optimization of the active layers for organic optoelectronic applications. A thermal annealing treatment to improve and stabilize the morphology of the active layer after solution casting is common practice and usually carried out at a

rather high temperature, in a window between 100 and 150 °C.[24,26] The chosen annealing temperature and duration are mostly defined by trial and error, or inspired by previous studies, and certainly not rationally optimized in all cases. A scientific understanding of the effectivity of thermal annealing can be given by the underlying state diagram and is further illustrated for the three model systems in Figure 8. The T-resolved SAXS and WAXS heating results of 20:80 w/w% mixtures are shown after an *isothermal treatment for 30 min*, followed by a cooling at 500 K min^{-1} to 25 °C in RHC. The 20:80 w/w% composition, with an excess of $PC_{61}BM$ against the pure co-crystal composition, was chosen because it is corresponding to a more commonly used ratio in devices. The isothermal temperatures for each system (indicated in Figure 3 (g-i)) were chosen equal to the respective onset temperatures of crystallization, $T_{c,onset}$, during non-isothermal cooling in RHC (see Figure S3), in order to promote co-crystallization, a feature desired for example in cavity enhanced PBTTT:$PC_{61}BM$ OPDs, as it leads to enhanced CT absorption.[23] Upon heating from room temperature, isothermally treated mixtures of PBTTT:$PC_{61}BM$ and PBTTT-OR-R:$PC_{61}BM$ show a similar response as after a *non-isothermal cooling* from the melt at 20 K min^{-1} (compare to Figure 6 (a',b',c')), i.e. incongruent melting of pure co-crystals with formation of $PC_{61}BM$ crystals in combination with an excess of $PC_{61}BM$ from room temperature for the 20:80 w/w% composition. Whereas the SAXS patterns don't indicate loss of co-crystal quality, but without co-crystal perfectioning, the WAXS patterns show more pronounced $PC_{61}BM$ peaks. This likely results from a coarsening process in which initially small and defective $PC_{61}BM$ crystals transform into bigger ones ($PC_{61}BM$ crystal perfectioning). Note that PBTTT and PBTTT-OR-R cannot crystallize in these conditions, as the chosen isothermal temperatures are beyond the liquidus lines of the respective polymers (indicated in Figure 3 (g,h)). On the other hand, the 20:80 w/w% mixture of PBTTT-$(OR)_2$:$PC_{61}BM$ shows that, besides the expected diffractions of co-crystals and $PC_{61}BM$ crystals, also the diffractions of PBTTT-$(OR)_2$ polymer crystals are observed from 25 °C on (see white arrow in Figure 8). As this mixture of PBTTT-$(OR)_2$:$PC_{61}BM$, with 80 w% of $PC_{61}BM$, does not contain excess of polymer, this result suggests that the isothermal treatment at 210 °C ($T_{c,onset}$ of non-isothermal co-crystallization in RHC) promotes the separate crystallization of $PC_{61}BM$ *and* PBTTT-$(OR)_2$ at the expense of co-crystallization. This can be understood considering the XRD results of Figure 7 (in

non-isothermal cooling), and taking into account the shape and relative position of the liquidus lines of PBTTT-$(OR)_2$, $PC_{61}BM$, and the co-crystals, as indicated in the phase diagram of Figure 3 (i). Indeed, the isothermal treatment at 210 °C for the 20:80 w/w% mixture was performed well below the liquidus line of PBTTT-$(OR)_2$, allowing crystallization as already observed in non-isothermal conditions around that temperature (see Figure 7). In this way, the isothermal crystallization of PBTTT-$(OR)_2$ is enriching the remaining liquid mixture in $PC_{61}BM$, and thus also promoting isothermal crystallization of the latter well below its liquidus line. Note that for this 20:80 w/w% mixture, isothermal crystallization might be initiated with $PC_{61}BM$, enriching the remaining liquid mixture in polymer and inducing isothermal crystallization of the latter. This mutual interaction of both components on their separate crystallization is not only influenced by the chosen mixture composition, but also by their relative supercooling (much larger for $PC_{61}BM$ than for the polymer). Anyway, the separate isothermal crystallization of $PC_{61}BM$ *and* PBTTT-$(OR)_2$ at 210 °C finally leads to a suppression of co-crystallization at 210 °C and also in the subsequent cooling to 25 °C. These results are in line with the state/phase diagram of PBTTT-$(OR)_2$:$PC_{61}BM$ with a eutectic between PBTTT-$(OR)_2$ and $PC_{61}BM$ beyond 280 °C (*vide supra*). The latter case demonstrates that the applied thermal treatment is not beneficial to promote co-crystallization. Note that this isothermal treatment at 210 °C is also favoring separate crystallization of $PC_{61}BM$ *and* PBTTT-$(OR)_2$ at the expense of co-crystallization for a 45:55 w/w% composition of PBTTT-$(OR)_2$:$PC_{61}BM$, as illustrated in Figure S10, which is again in line with the phase diagram of PBTTT-$(OR)_2$:$PC_{61}BM$ of Figure 3 (i). The T-resolved SAXS and WAXS results of Figure 8 are of importance for the fabrication of NIR-OPD devices using 20:80 w/w% mixtures of either of the three model systems as active layers. The chosen isothermal treatments suggest that, while beneficial for PBTTT:$PC_{61}BM$ and PBTTT-OR-R:$PC_{61}BM$, co-crystallization could be suppressed in PBTTT-$(OR)_2$:$PC_{61}BM$, which may negatively influence device performance of the latter system in case of OPDs relying on strong CT absorption (and thus a large amount of donor-acceptor interface). The state diagrams of Figure 3 give a rationale for these opposite effects and can help selecting appropriate thermal conditions for each system.

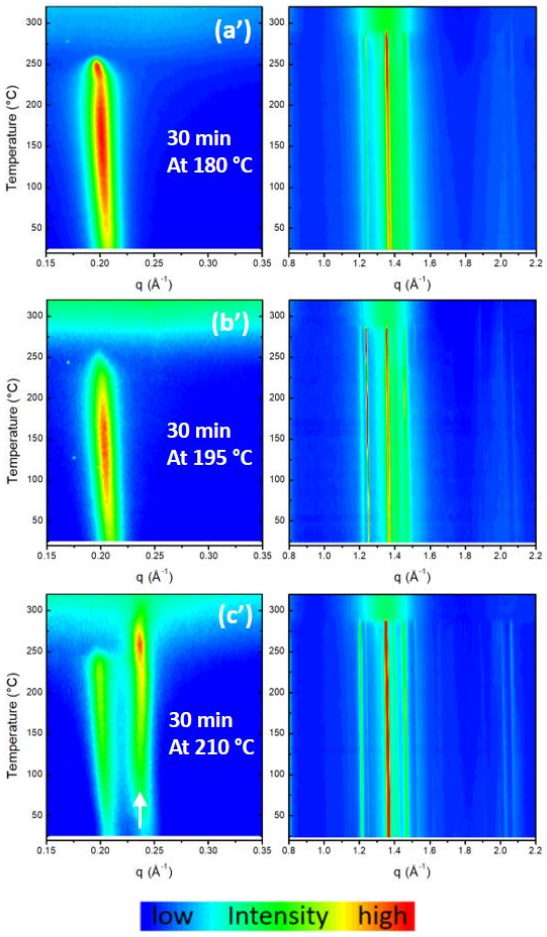

Figure 8. Temperature-resolved synchrotron SAXS and WAXS heating patterns for 20:80 w/w% (a',b',c') mixtures of (a') PBTTT:$PC_{61}BM$, (b') PBTTT-OR-R:$PC_{61}BM$, and (c') PBTTT-$(OR)_2$:$PC_{61}BM$. Heating at 50 K min^{-1} from 25 °C to 320 °C (Linkam) after an *isothermal treatment* from the melt at a given temperature, indicated on each graph, for 30 min (RHC). The color scale bar is indicative for the relative increasing intensity of the diffraction patterns (from blue to red). The white arrow in (c') indicates the presence of PBTTT-$(OR)_2$ crystals from 25 °C on. Note that the labeling (a',b',c') is referring at (a',b',c') of Figure 6.

Homocoupling defects – Influence on isothermal treatments and state diagrams

The beneficial effect of isothermal treatment at the device level was also demonstrated recently.[27] After a thermal annealing for 30 minutes at 150 and 200 °C, EQE analysis and optical microscopy done for PBTTT-OR-R:$PC_{61}BM$ bulk heterojunction photodiodes confirmed the stability of the intercalated polymer:fullerene active layer morphology, containing thermally robust co-crystals of homocoupling-free PBTTT-OR-R (for 45:55 and 20:80 w/w% compositions) in combination with coarsened excess $PC_{61}BM$ crystals (for 20:80 w/w% compositions).[27] These results on the device level are consistent with the corresponding state diagram of PBTTT-OR-R:$PC_{61}BM$ as shown in Figure 3 (h). However, for

photodiodes containing classical Stille-polymerized PBTTT-OR-R:$PC_{61}BM$ mixtures, the same analysis at identical conditions showed that the device performance was severely deteriorated.[27] This striking difference with the homocoupling-free system was attributed to the much lower thermal stability of the co-crystal as a result of the substantial amount (19%) of homocoupling defects in the Stille variant.[26,27] This discrepancy can now be rationalized in terms of the state diagram of Stille-polymerized PBTTT-OR-R:$PC_{61}BM$.

This state diagram was constructed in a similar way as discussed above for the homocoupling-free systems by means of RHC and T-resolved XRD experiments for different compositions. $T_{m,endset}$ values for PBTTT-OR-R backbones, co-crystals, and $PC_{61}BM$ from RHC thermograms and T-resolved diffraction peaks were used to characterize the liquidus lines of the different crystalline phases. The corresponding $T_{m,endset}$ – composition plots give rise to the state diagram based on RHC (Figure 9 (a)) and XRD (Figure 9 (b)). Both data sets are again in good agreement, except for a systematically higher absolute temperature assignment observed for RHC (*vide supra*). Note that $T_{m,endset}$ of the co-crystals, as observed in Figure 9 (b), is hidden in Figure 9 (a) in the melting trajectories of the polymer (see Figure S11). Compared to the state diagram of the homocoupling-free PBTTT-OR-R system, as shown in Figure 3 (b) for RHC and Figure 3 (e) for XRD, a striking difference is noticed regarding the thermal stability of the co-crystal. While the melting point depression for PBTTT-OR-R nearly starts from the same $T_{m,endset}$ value in the presence or absence of homocoupling, the $T_{m,endset}$ values for the co-crystal of Stille-polymerized PBTTT-OR-R (at 230 °C or lower) are at least 40 K lower than for PBTTT-OR-R without defects (around 270 °C). This lowering of the co-crystal liquidus line against the liquidus lines of PBTTT-OR-R and $PC_{61}BM$ is schematically indicated by the downward arrow in Figure 3 (h). The change in the positioning of the liquidus lines switches the shape of the state diagram from *PBTTT-like*, with one eutectic between the polymer and co-crystal and incongruent melting of the co-crystal for $PC_{61}BM$-rich compositions, toward *PBTTT-(OR)$_2$-like*, with one eutectic between the polymer and $PC_{61}BM$ at a temperature beyond the liquidus line of the co-crystal which is stable at lower

temperatures by means of a reversible liquid crystalline polymer-co-crystal 'solid-solid' transformation (*vide supra*).

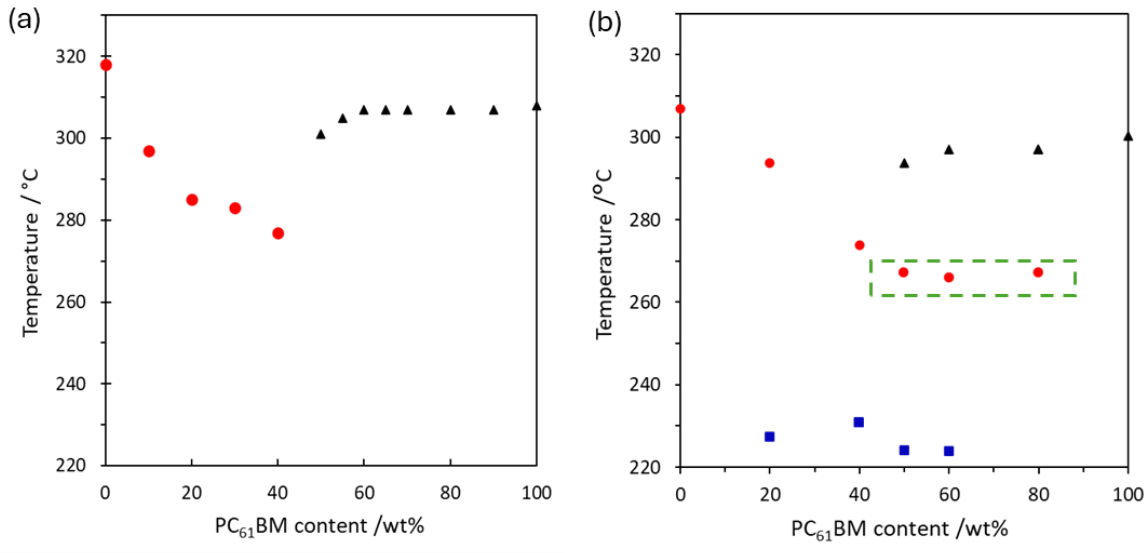

Figure 9. State diagram of Stille-polymerized PBTTT-OR-R:$PC_{61}BM$ based on (a) $T_{m,endset}$ values from the RHC thermograms of Figure S11 and (b) endset values of T-resolved XRD. Endset values for Stille-polymerized backbones, co-crystals, and $PC_{61}BM$ are indicated with red circles, blue squares, and black triangles (full symbols), respectively. $T_{m,endset}$ of the co-crystals in (a) is hidden in the melting trajectories of the polymer and/or crystallization of $PC_{61}BM$. The red circles at constant temperature in the dashed green box in (b) represent melting of the Stille-polymerized PBTTT-OR-R in the eutectic phase.

In summary, not only the nature of the PBTTT derivative (without defects) but also the amount of homocoupling defects in the same type of material can have a profound effect on the state diagram and therefore also on well-chosen isothermal annealing conditions. This effect is clear for PBTTT-OR-R. In case of Stille-polymerized PBTTT, with substantially less homocoupling defects (likely <5%), this effect is not noticeable (data not shown). In case of the highest amount of defects (26%) in Stille-polymerized PBTTT-$(OR)_2$, the co-crystal is no longer formed and the double binary state diagram can no longer be established.[26]

3. Conclusions

The true structure of alternating conjugated polymers applied as state-of-the-art active materials for a number of organic electronics applications is often neglected, although in many cases it deviates from the theoretical repeating unit by the presence of molecular defects such as homocouplings.[25,26] A non-reproducible amount of defects from batch to batch causes changes in the properties of these alternating polymers and their mixtures with small acceptor molecules such as fullerenes. Increased attention to synthesize defect-free alternating polymers is therefore justified, not only from the perspective of developing reliable electronic devices with an improved and stable performance but also to allow the establishment of correct structure-processing-property relationships for these systems.

This approach, using regular chemical structures without defects in the alternating donor-acceptor sequence of the conjugated polymer backbones, resulted in the construction of novel double binary state diagrams of three model systems, PBTTT:$PC_{61}BM$, PBTTT-OR-R:$PC_{61}BM$, and PBTTT-$(OR)_2$:$PC_{61}BM$. They were constructed using RHC and T-resolved synchrotron XRD results of oxidatively synthesized homocoupling-free alternating polymers mixed with $PC_{61}BM$ in a wide range of compositions. The experimental data were qualitatively compared to calculations based on the Flory-Huggins theory for the liquid mixture state and standard thermodynamic models for the crystalline state of the pure components and the co-crystal. Co-crystallization between the conjugated polymer and $PC_{61}BM$ always occurred, giving rise to co-crystals of 45:55 w/w% mixing ratio which remained stable up to high temperatures (260–280 °C) in a wide composition range. It was proven for the first time that all co-crystals show *incongruent (peritectic)* melting. While for the co-crystals the incongruent melting transition was highest for the PBTTT:$PC_{61}BM$ co-crystal, the congruent melting temperature of pure PBTTT, PBTTT-OR-R, and PBTTT-$(OR)_2$ increased with alkoxy substitution, so as a result of the chemistry of the side chains and not because of a different amount of defects in the backbones.[26,27] These relative changes between polymer and corresponding co-crystal allowed a systematic study of their double binary state diagrams. All state diagrams show *one eutectic*, i.e. between polymer and co-

crystal in the case of PBTTT and PBTTT-OR-R, and between polymer and $PC_{61}BM$ for PBTTT-$(OR)_2$. The latter eutectic of the PBTTT-$(OR)_2$:$PC_{61}BM$ system beyond 280 °C leads to a reversible 'solid-solid' transformation from liquid crystalline PBTTT-$(OR)_2$ and $PC_{61}BM$ towards co-crystal in cooling, and from co-crystal towards liquid crystalline PBTTT-$(OR)_2$ and $PC_{61}BM$ in heating. The mobile side chain fraction in the liquid crystalline state of PBTTT-$(OR)_2$ seems crucial for this reversible transformation.

Finally, an isothermal instead of a non-isothermal pathway was evaluated for the three model systems. The isothermal treatment was chosen at the onset temperature during non-isothermal cooling. While beneficial for PBTTT:$PC_{61}BM$ and PBTTT-OR-R:$PC_{61}BM$ regarding co-crystal formation without loss of quality in combination with $PC_{61}BM$ perfectioning, the $PC_{61}BM$-rich mixtures of PBTTT-$(OR)_2$:$PC_{61}BM$ showed a suppression of co-crystallization with formation of separate crystals of PBTTT-$(OR)_2$ and $PC_{61}BM$. The latter effect might be negative for PBTTT-$(OR)_2$:$PC_{61}BM$ photodetector performance by suppressing the charge-transfer absorption.[6,7] The same detrimental effect was observed for classical Stille-polymerized PBTTT-OR-R, containing 19% of homocoupling defects. Such opposing effects of a thermal treatment can be explained by the shape and the position of the liquidus lines of the state diagrams, highlighting their strong added value in selecting an efficient annealing step during device optimization. The extension of this rational approach to other state-of-the-art systems in the field of organic electronics seems feasible, at least if conjugated electron donating and electron accepting organic semiconductors of sufficient crystallinity are involved.

4. Methods section

Materials

- Pure polymers and $PC_{61}BM$

The homocoupling-free donor polymers PBTTT (M_n = 26.0 kg mol^{-1}, M_w = 70.6 kg mol^{-1}, $Đ$ = 2.7), PBTTT-OR-R (M_n = 24.4 kg mol^{-1}, M_w = 80.7 kg mol^{-1}, $Đ$ = 3.3), and PBTTT-$(OR)_2$ (M_n = 13.2 kg mol^{-1}, M_w = 23.9 kg mol^{-1}, $Đ$ = 1.8) were synthesized by oxidative polymerization and characterized as reported in previous work.[26,27] The Stille variant of PBTTT-OR-R was synthesized and characterized as reported in

previous work.[27] The acceptor material $PC_{61}BM$ (with a purity of 99 %) was purchased from Solenne and used without further purification.

- *Preparation of polymer:$PC_{61}BM$ mixtures*

All the samples for RHC and synchrotron XRD analysis were prepared in a systematic way. The polymer:$PC_{61}BM$ solutions (6 mg mL^{-1}) were prepared by dissolving polymer:$PC_{61}BM$ mixtures of different compositions into chlorobenzene. These solutions were stirred at 80 °C and drop-casted on a glass substrate at 80 °C. After 24 hours of drying at room temperature, the mixtures were removed from the substrate by scratching.

Experimental techniques

- *Thermogravimetric Analysis*

Thermogravimetric analysis (TGA) was performed on a TA instruments TGA Q5000. Measurements were performed at a heating rate of 20 K min^{-1} using Nitrogen (25 mL min^{-1}) as purge gas. Sample masses of approximately 1 mg were used.

- *Rapid Heat-Cool Differential Scanning Calorimetry*

Thermal analysis was performed using Rapid Heat-Cool Differential Scanning Calorimetry (RHC), which is a prototype instrument developed by TA instruments.[35,36] Calibration of temperature and enthalpy was performed by using indium standards at 500 K min^{-1}. Dedicated aluminum RHC crucibles were filled with samples of around 200–250 µg. Experiments were performed with Nitrogen (6 mL min^{-1}) as purge gas.

- *Temperature-Resolved Synchrotron X-ray Diffraction*

The experimental details for the temperature-resolved synchrotron X-ray diffraction experiments were described in detail elsewhere.[26,27]

Theoretical calculations

The liquidus lines in the double binary phase diagrams of Figure 3 (g-i) were calculated according to a thermodynamic equilibrium model, describing the heterogeneous equilibrium between a

homogeneous binary mixture in the liquid phase (Flory-Huggins theory) and the pure crystalline phase of component *i* of the mixture. More details are given in the Supporting Information.

Supporting Information

Supporting Information is available from the Wiley Online Library or from the author.

Acknowledgements

The authors thank the Research Foundation – Flanders (FWO Vlaanderen) for financial support (Ph.D. project 1S50822N, project G0B2718N and DUBBLE project I001919N).

Received: ((will be filled in by the editorial staff))
Revised: ((will be filled in by the editorial staff))
Published online: ((will be filled in by the editorial staff))

References

[1] A. Wadsworth, Z. Hamid, J. Kosco, N. Gasparini, I. McCulloch, *Adv. Mater.* **2020**, *32*, 2001763.

[2] O. Almora, D. Baran, G. C. Bazan, C. I. Cabrera, S. Erten-Ela, K. Forberich, F. Guo, J. Hauch, A. W. Y. Ho-Baillie, T. J. Jacobsson, R. A. J. Janssen, T. Kirchartz, N. Kopidakis, M. A. Loi, R. R. Lunt, X. Mathew, M. D. McGehee, J. Min, D. B. Mitzi, M. K. Nazeeruddin, J. Nelson, A. F. Nogueira, U. W. Paetzold, B. P. Rand, U. Rau, H. J. Snaith, E. Unger, L. Vaillant-Roca, C. Yang, H. Yip, C. J. Brabec, *Adv. Energy Mater.* **2023**, *13*, 2203313.

[3] H. Bronstein, C. B. Nielsen, B. C. Schroeder, I. McCulloch, *Nat. Rev. Chem.* **2020**, *4*, 66.

[4] O. Ostroverkhova, *Chem. Rev.* **2016**, *116*, 13279.

[5] T. M. Burke, S. Sweetnam, K. Vandewal, M. D. McGehee, *Adv. Energy Mater.* **2015**, *5*, 1500123.

[6] K. Vandewal, *Annu. Rev. Phys. Chem.* **2016**, *67*, 113.

[7] B. Siegmund, A. Mischok, J. Benduhn, O. Zeika, S. Ullbrich, F. Nehm, M. Böhm, D. Spoltore, H. Fröb, C. Körner, K. Leo, K. Vandewal, *Nat. Commun.* **2017**, *8*, 15421.

[8] N. Cates, E. Cho, R. Gysel, C. Risko, V. Coropceanu, C. E. Miller, S. Sweetnam, A. Sellinger, M. Heeney, I. McCulloch, J. Brédas, M. F. Toney, M. D. McGehee, *Adv. Energy Mater.* **2012**, *2*, 1208.

[9] B. A. Collins, E. Gann, L. Guignard, X. He, C. R. McNeill, H. Ade, *J. Phys. Chem. Lett.* **2010**, *1*, 3160.

[10] L. Ye, H. Hu, M. Ghasemi, T. Wang, B. A. Collins, J.-H. Kim, K. Jiang, J. H. Carpenter, H. Li, Z. Li, T. McAfee, J. Zhao, X. Chen, J. L. Y. Lai, T. Ma, J.-L. Bredas, H. Yan, H. Ade, *Nat. Mater.* **2018**, *17*, 253.

[11] S. T. Turner, P. Pingel, R. Steyrleuthner, E. J. W. Crossland, S. Ludwigs, D. Neher, *Adv. Funct. Mater.* **2011**, *21*, 4640.

[12] B. A. Collins, Z. Li, J. R. Tumbleston, E. Gann, C. R. Mcneill, H. Ade, *Adv. Energy Mater.* **2013**, *3*, 65.

[13] W. Yin, M. Dadmun, *ACS Nano* **2011**, *5*, 4756.

[14] L. Ye, B. A. Collins, X. Jiao, J. Zhao, H. Yan, H. Ade, *Adv. Energy Mater.* **2018**, *8*, 1703058.

[15] N. C. Cates, R. Gysel, J. E. P. Dahl, A. Sellinger, M. D. McGehee, *Chem. Mater.* **2010**, *22*, 3543.

[16] A. C. Mayer, M. F. Toney, S. R. Scully, J. Rivnay, C. J. Brabec, M. Scharber, M. Koppe, M. Heeney, I. McCulloch, M. D. McGehee, *Adv. Funct. Mater.* **2009**, *19*, 1173.

[17] N. C. Miller, E. Cho, R. Gysel, C. Risko, V. Coropceanu, C. E. Miller, S. Sweetnam, A. Sellinger, M. Heeney, I. McCulloch, J. L. Brédas, M. F. Toney, M. D. McGehee, *Adv. Energy Mater.* **2012**, *2*, 1208.

[18] M. A. White, R. T. Perry, *Chem. Mater.* **1994**, *6*, 603.

[19] J. M. Guenet, *Macromol. Symp.* **2007**, *258*, 179.

[20] I. McCulloch, M. Heeney, C. Bailey, K. Genevicius, I. MacDonald, M. Shkunov, D. Sparrowe, S. Tierney, R. Wagner, W. Zhang, M. L. Chabinyc, R. J. Kline, M. D. McGehee, M. F. Toney, *Nat. Mater.* **2006**, *5*, 328.

[21] F. C. Jamieson, E. B. Domingo, T. McCarthy-Ward, M. Heeney, N. Stingelin, J. R. Durrant, *Chem. Sci.* **2012**, *3*, 485.

[22] N. C. Miller, E. Cho, M. J. N. Junk, R. Gysel, C. Risko, D. Kim, S. Sweetnam, C. E. Miller, L. J. Richter, R. J. Kline, M. Heeney, I. McCulloch, A. Amassian, D. Acevedo-Feliz, C. Knox, M. R. Hansen, D. Dudenko, B. F. Chmelka, M. F. Toney, J. L. Brédas, M. D. McGehee, *Adv. Mater.* **2012**, *24*, 6071.

[23] Z. Tang, Z. Ma, A. Sánchez-Díaz, S. Ullbrich, Y. Liu, B. Siegmund, A. Mischok, K. Leo, M. Campoy-Quiles, W. Li, K. Vandewal, *Adv. Mater.* **2017**, *29*, 1702184.

[24] J. Vanderspikken, Q. Liu, Z. Liu, T. Vandermeeren, T. Cardeynaels, S. Gielen, B. Van Mele, N. Van den Brande, B. Champagne, K. Vandewal, W. Maes, *Adv. Funct. Mater.* **2022**, *32*, 2108146.

[25] G. Pirotte, P. Verstappen, D. Vanderzande, W. Maes, *Adv. Electron. Mater.* **2018**, *4*, 1700481.

[26] J. Vanderspikken, Z. Liu, X. Wu, O. Beckers, S. Moro, T. J. Quill, Q. Liu, A. Goossens, A. Marks, K. Weaver, M. Hamid, B. Goderis, E. Nies, V. Lemaur, D. Beljonne, A. Salleo, L. Lutsen, K. Vandewal, B. Van Mele, G. Costantini, N. Van den Brande, W. Maes, *Adv. Funct. Mater.* **2023**, 2309403.

[27] Z. Liu, J. Vanderspikken, P. Mantegazza, S. Moro, M. Hamid, S. Mertens, N. Van den Brande, L. Lutsen, V. Lemaur, D. Beljonne, G. Costantini, K. Vandewal, B. Van Mele, W. Maes, B. Goderis, *Adv. Funct. Mater.* **2024**, 2413647.

[28] N. Van den Brande, M. Defour, D. Devisscher, P. Verstappen, G. Reekmans, J. D'Haen, P.

Adriaensens, W. Maes, G. Van Assche, B. Van Mele, *J. Phys. Chem. C* **2020**, *124*, 7566.

[29] M. Defour, N. Van den Brande, L. Van Lokeren, G. Van Assche, W. Maes, D. Vanderzande, B. Van Mele, *RSC Adv.* **2016**, *6*, 92981.

[30] N. Van den Brande, G. Van Assche, B. Van Mele, *Polym. Int.* **2019**, *68*, 277.

[31] N. Cates, R. Gysel, C. E. Miller, E. Verploegen, Z. Beiley, M. Heeney, I. McCulloch, Z. Bao, M. F. Toney, M. D. McGehee, *J. Polym. Sci. Part B Polym. Phys.* **2011**, *49*, 499.

[32] C. Müller, T. A. M. Ferenczi, M. Campoy-Quiles, J. M. Frost, D. D. C. Bradley, P. Smith, N. Stingelin-Stutzmann, J. Nelson, *Adv. Mater.* **2008**, *20*, 3510.

[33] L. Zhang, H. Li, K. Zhao, T. Zhang, D. Liu, S. Wang, F. Wu, Q. Zhang, Y. Han, *Polymer* **2022**, *256,* 125178.

[34] R. Koningsveld, W. H. Stockmayer, E. Nies, *Polymer Phase Diagrams: A Textbook*, Oxford University Press, **2001**.

[35] R. L. Danley, P. A. Caulfield, S. R. Aubuchon, *Am. Lab.* **2008**, *41*, 9.

[36] S. Wouters, F. Demir, L. Beenaerts, G. Van Assche, *Thermochim. Acta* **2012**, *530*, 64.